GEOPHYSICS, VOL. 82, NO. 6 (NOVEMBER-DECEMBER 2017); P. MR191–MR200, 11 FIGS., 2 TABLES.
10.1190/GEO2017-0171.1

Anisotropic surface-wave characterization of granular media

Edan Gofer[1], Ran Bachrach[2], and Shmuel Marco[3]

ABSTRACT

In unconsolidated granular media, the state of stress has a major effect on the elastic properties and wave velocities. Effective media modeling of granular packs shows that a vertically oriented uniaxial state of stress induces vertical transverse isotropy (VTI), characterized by five independent elastic parameters. The Rayleigh wave velocity is sensitive to four of these five VTI parameters. We have developed an anisotropic Rayleigh wave inversion that solves for four of the five independent VTI elastic parameters using anisotropic Thomson-Haskell matrix equations that can be used to determine the degree of anisotropy and the state of stress in granular media. The proposed method incorporates an initial model search guided by rock-physics models and dispersion curve inversion that uses a gradient-based solver. We carried out the inversion on a synthetic example and a real data set in which we inverted for in situ elastic moduli of unconsolidated sands at very low effective stress. The synthetic data example results showed that we are able to correctly estimate the granular media's effective elastic moduli. When the inversion was carried out with real data, the results indicate that the sand at very low effective stress is elastically anisotropic and that it is stiffer along the vertical axis than the horizontal axis. Furthermore, our results are in agreement with past studies related to granular media.

INTRODUCTION

Elastic-wave velocities in unconsolidated sediments vary with stress (Bachrach et al., 1998; Zimmer et al., 2002). Although the stress field in granular media is heterogeneous and complex (Geng et al., 2001), effective media modeling of granular sands tries to associate an average stress field that represents the average sediment response. Therefore, analysis of seismic waves in granular media can help to determine the effective elastic properties from which we may be able to estimate the state of stress in media such as sands.

In the case of self-loading granular media, one can consider two simplified states of stress: a hydrostatic state and a triaxial stress state. In the latter, the vertical stress is much greater than the maximum and the minimum horizontal stresses. Unconsolidated sands, subject to a state of stress loading where the vertical stress is greater than horizontal stress, develop larger elastic moduli in the direction of the applied stress relative to elastic moduli in the perpendicular direction; therefore, the media is anisotropic. Stress-induced anisotropy has been observed in many laboratory and theoretical studies (Nur and Simmones, 1969; Walton, 1987; Sayers, 2002). In contrast, granular media under hydrostatic loading is statistically isotropic.

Surface waves sample the shallow subsurface with varying wavelengths. High frequencies (short wavelengths) sample the very shallow part of the sedimentary column, whereas low frequencies (long wavelengths) penetrate deeper into the ground. Surface-wave dispersion occurs when velocity varies with depth (Aki and Richards, 1980). Note that the surface-wave velocity is related to the media's structure in a complex manner. The surface-wave phase-velocity dispersion curve is usually modeled using the Thomson-Haskell method (Thomson, 1950; Haskel 1953). The method models surface-wave phase velocities in a horizontally stratified media, and it is commonly used as the forward model operator in Rayleigh and Love wave inversions.

Seismic characterization of unconsolidated granular media has been the focus of several published works. Bachrach et al. (1998) estimate a beach sand in situ P-wave (V_P) and S-wave (V_S) velocity profile based on first-arrival analysis. Jacob et al. (2008) carry out a laboratory experiment in which dispersion curves of guided acoustic surface modes were inverted to solve for P- and S-wave velocities in a pack of uniformly sized glass beads in a Plexiglas box. Bodet et al. (2010) extend the work of Jacob et al. (2008) and carry

Manuscript received by the Editor 16 March 2017; revised manuscript received 26 July 2017; published online 06 October 2017.
[1]Tel Aviv University, Department of Geophysics, Tel Aviv, Israel and Schlumberger, Houston, Texas, USA. E-mail: edangofe@post.tau.ac.il; egofer@slb.com.
[2]Schlumberger, Houston, Texas, USA. E-mail: rbachrach@slb.com.
[3]Tel Aviv University, Department of Geophysics, Tel Aviv, Israel. E-mail: shmulikm@tau.ac.il.

out a surface-wave inversion to estimate the V_S profile. Gofer and Bachrach (2012) carry out Rayleigh wave Bayesian inversion to estimate an in situ 1D S-wave velocity model in a thick Aeolian sand dune. Bergamo and Socco (2016) carry out a multimode surface-wave inversion on synthetic and real data, showing the uplift of using higher modes when trying to solve for V_S and V_P models in unconsolidated sands.

Theoretical effective medium models assume a granular pack of identical perfect spheres. These models predict that the effective elastic moduli have a pressure power dependence of 1/3 (Digby, 1981; Walton, 1987). The aforementioned published work either solved for the P- and S-wave velocity model assuming the pressure dependency of 1/3 or solved jointly for P- and S-wave velocities and the pressure power dependency. Moreover, in each case, a hydrostatic state of stress was assumed. Gofer and Bachrach (2013) investigate the effects of a uniaxial stress field, caused by vertical loading on surface-wave phase velocity. Their results show similarities between dispersion curves from a field experiment on a sand dune and a synthetic model of granular media under a uniaxial stress state. This suggests that, in a sand dune, the vertical stress is greater than the horizontal stress.

In this study, we explore the effect that anisotropy has on Rayleigh wave phase velocities using the Thomson-Haskell matrix for vertical transverse isotopic (VTI) media. It should be noted that VTI equations for horizontally stratified media for Rayleigh and Love waves were derived in the past by Anderson (1961) and Ke et al. (2011). In this study, we present another derivation of VTI equations. The equations are detailed in Appendix A. We also investigate anisotropic surface-wave inversion for granular media and explore the model parameters' uncertainty of the elastic moduli. Finally, we show results from a synthetic example and a real data set example of anisotropic Rayleigh wave inversion.

THOMSON-HASKELL METHOD FOR VTI MEDIA

Elastic wave propagation in a stratified media can be solved through a boundary value problem. The problem can be posed as a finite number of linear first-order differential equations with variable coefficients. The solution of such a system composed of motion-stress equations can be presented using the product integral (also known as the propagator) of the coefficients' matrix (Gilbert and Backus, 1966). The Thomson-Haskell method uses this system to solve the dispersion of Rayleigh and Love waves under the approximation of stratified media made of homogeneous layers. The first-order differential P-SV wave motion stress equations can be defined by

$$\frac{d\mathbf{f}(z)}{dz} = \mathbf{A}(z)\mathbf{f}(z), \tag{1}$$

where

$$\mathbf{A}(z) = \begin{bmatrix} 0 & k & C_{44}(z)^{-1} & 0 \\ -kC_{13}(z)C_{33}(z)^{-1} & 0 & 0 & C_{33}(z)^{-1} \\ k^2(C_{11}(z) - C_{13}(z)^2C_{33}(z)^{-1}) - \omega^2\rho & 0 & 0 & kC_{13}(z)C_{33}(z)^{-1} \\ 0 & -\omega^2\rho & -k & 0 \end{bmatrix}, \tag{2}$$

where ω is the angular frequency, ρ is the density, k is the horizontal wavenumber, and C_{ij} are the elastic stiffness parameters of a VTI media and the indices represent Voigt notations

$$\mathbf{f}(z) = [u, w, \sigma_{zx}, \sigma_{zz}]^T, \tag{3}$$

where u and w are the horizontal and vertical displacement components, respectively, and σ_{xz} and σ_{zz} are the stress components. Given that each layer in the stratified media is homogeneous, the motion-stress vector at the bottom of the layer can be defined as a function of the motion-stress vector at the top of the layer as

$$\mathbf{f}(z) = \mathbf{G}(z, z_0)\mathbf{f}(z_0), \tag{4}$$

where

$$\mathbf{G}(z, z_0) = e^{(z-z_0)\mathbf{A}(z)}, \tag{5}$$

where $\mathbf{G}$, defined in Appendix A, is based on the eigenvector matrix of matrix $\mathbf{A}$ (Aki and Richards, 1980). Applying continuity of displacement and stress at the interfaces between layers, we can express the relationship between the free surface and the bottom layer with the propagator matrix as

$$\mathbf{f}(z_n) = \mathbf{P}(z_n, z_0)\mathbf{f}(z_0) = \mathbf{G}_{n-1} \ldots \mathbf{G}_2\mathbf{G}_1\mathbf{f}(z_0). \tag{6}$$

Subscript n indicates the number of the layer in the stratified media.

The Rayleigh wave is the nontrivial solution of the P-SV wavefield along a surface between the air and a solid. Given the boundary conditions of zero stress at the free surface and no upgoing wave coming from the bottom half-space, the nontrivial solution must satisfy

$$\begin{bmatrix} P^{\backslash} \\ S^{\backslash} \\ 0 \\ 0 \end{bmatrix} = \mathbf{F}_{n+1}^{-1}\mathbf{P}(z_n, z_0)\mathbf{f}(z_0) = \mathbf{B}\mathbf{f}(z_0), \tag{7}$$

where $\mathbf{F}$ is the solution of the eigenvalue problem of matrix $\mathbf{A}$ (Appendix A). The nontrivial solution for a given stack of homogeneous horizontal layers exists for pairs of angular frequency and horizontal wavenumbers that satisfies

$$\begin{vmatrix} B_{31} & B_{32} \\ B_{41} & B_{42} \end{vmatrix} = 0, \tag{8}$$

where B represent elements in matrix $\mathbf{B}$. Matrix $\mathbf{B}$ is a 4×4 matrix, and the subscripts in equation 8 represent the row and column indices, respectively.

STRESS-STATE EFFECT ON DISPERSION CURVE

Following Walton (1987), unconsolidated granular media in a state of hydrostatic stress are statistically isotropic. Therefore, the effective elastic stiffness tensor for these media can be represented using two effective elastic moduli: the bulk modulus and the shear modulus. When the same granular pack is subjected to uniaxial compression, the medium is statistically transversely isotopic, which can be described by five independent elastic constants: C_{11}, C_{33}, C_{44}, C_{66}, and C_{13}. The elastic moduli are dependent on the porosity of the medium, the coordination number, and the effective stress. In both states of stress, the elastic moduli have a power-law dependency on stress of 1/3. The Walton (1987) effective elastic moduli are explicitly detailed in Appendix B. Assuming that the vertical effective stress is

the overburden stress, we can calculate the stiffness matrix and the effective elastic moduli at each depth point for uniaxial and/or hydrostatic loading conditions.

To investigate the effect of the state of stress in granular media on the Rayleigh wave dispersion curve, we model a medium that is made of perfectly round and smooth grains of quartz with a porosity of 37% and average coordination number of four. For simplicity, we assume that the stress is only depth-dependent (no change in density or porosity as a function of depth, an assumption consistent with sand dunes or beach sand at the near surface). Note that as the effective stress increases with depth, the effective elastic moduli at each depth level increase. This leads to the depth-dependent effective elastic stiffness tensor shown in Figure 1 for a uniaxial state of stress. Note that the model in Figure 1 has Thomsen's (1986) VTI parameters ε and δ equal -0.31 and -0.35, respectively; ε is negative because overburden stress makes $C_{33} > C_{11}$. The calculated dispersion curves of the hydrostatic stress state model (blue line) and the uniaxial stress state model (red line) are shown in Figure 2. Surface-wave phase velocities are slower when we assume uniaxial loading. In this case, phase velocities are 35% slower because the average phase-velocity difference between the two models is 80 m/s. This difference is constant along the curves because both models assume the same power dependence in effective stress of 1/3. This difference between the curves shows how sensitive surface waves are to the stress state.

MODEL PARAMETER UNCERTAINTY ANALYSIS

The Rayleigh wave phase velocity can be written in its nonlinear implicit form:

$$R(f, k, C_{11}, C_{33}, C_{44}, C_{13}, \rho, h) = 0, \quad (9)$$

where f is the frequency and k is the horizontal wavenumber; C_{11}, C_{33}, C_{44}, and C_{13} are the elastic stiffness vectors; ρ is the density vector; and h is the layer thickness vector. The vectors contain the values of each parameter in every layer. In surface-wave inversion problems, we solve for properties of N number of layers given M number of picked phase velocities. In shallow unconsolidated dry granular medium where the effective elastic moduli can change rapidly as a function of depth, there is a need to discretize the medium to many layers. In this case, the inverse problem can become underdetermined. To reduce the model parameter space, we define model parameters that are a function of depth based on the effective medium theory of granular media where we assume that effective stress increases with depth z. Each elastic parameter is related to depth by

$$A_{11} = a_{11} z^{1/n}; A_{33} = a_{33} z^{1/n}; A_{44} = a_{44} z^{1/n}; A_{13} = a_{13} z^{1/n}, \quad (10)$$

where A_{ij} are the density normalized elastic stiffness parameters, which have velocity squared units; a_{11}, a_{33}, a_{44}, and a_{13} are the depth-independent coefficients of A_{11}, A_{33}, A_{44}, and A_{13}, respectively; and n is the power-law exponent. Also, the model parameter set we invert for is $\mathbf{m} = [a_{11}, a_{33}, a_{44}, a_{13}, n]^T$. The density is fixed and assumed to be known, as per our constant porosity assumption.

To understand our ability to solve for specific model parameters, we carry out an uncertainty analysis. We formulate the Rayleigh wave inverse problem as a Bayesian inverse problem, in which the posterior probability density function (PDF) is defined as $p(\mathbf{m}|\mathbf{d}) \propto p(\mathbf{d}|\mathbf{m})p(\mathbf{m})$, where $p(\mathbf{d}|\mathbf{m})$ is the likelihood and $p(\mathbf{m})$ is the prior. The objective function, assuming normal distribution, is a two-term objective function consisting of a data misfit term and a model prior misfit term (equation C-1). At the minimum of the objective function, the gradient of the function vanishes and the region

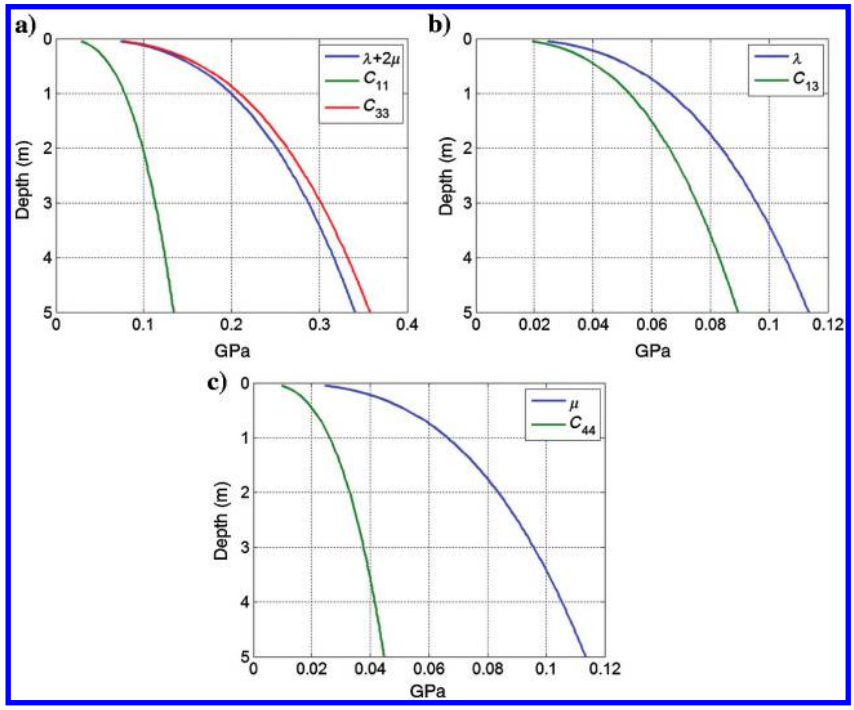

Figure 1. Effective Lamè parameter and shear modulus associated with hydrostatic stress state and effective elastic stiffness of the induced VTI response associated with the uniaxial stress state. (a) P-wave modulus, C_{11} and C_{33}, (b) Lamè parameter and C_{13}, and (c) shear modulus and C_{44}.

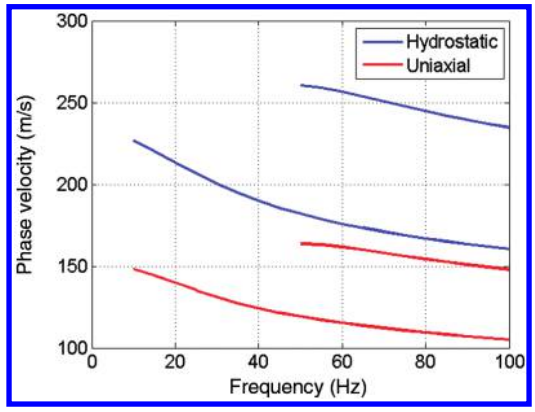

Figure 2. Rayleigh wave dispersion curves, fundamental mode, and first higher mode assuming a hydrostatic stress state (blue lines) and a uniaxial stress state (red lines).

is expressed with the Hessian (equations C-2 and C-3). Following Duijndam (1988), we approximate the N-dimensional ellipsoid shape around the minimum with eigenvalue decomposition to determine which parameters are well-resolved and which are poorly resolved. Well-resolved parameters are associated with high eigenvalues, and poorly resolved ones are related to low eigenvalues.

First, we plot (Figure 3) the eigenvectors and eigenvalues of the Hessian of the objective function defined in equation C-1 given that the observed Rayleigh wave dispersion curve includes only a fundamental mode. The picking error of the Rayleigh wave phase velocity V_f is assumed to have a normal distribution, where $V_f \sim N(V_f, 100)$. Prior model uncertainty is also assumed to have a normal distribution. We assume a variance of 0.2 km/s^2 for each of the depth-independent coefficients and variance of 0.2 for n. In the eigenvector matrix $\mathbf{V}$, we consider $\mathbf{V}_{ij}^T$ to be the jth cosine direction related to the jth model parameter and to the ith eigenvalue. Examining eigenvectors and eigenvalues in Figure 3, we can easily determine which model parameter is best resolved and which model parameter is the most difficult one to recover. We see that we are able to resolve well-model parameters a_{44} and n associated with the first and the second eigenvectors, respectively; a_{11} and a_{13} are related to eigenvectors 3 and 4. Eigenvalues 3 and 4 have the same order of magnitude, meaning that we can resolve the two parameters in an equal manner. In the fourth eigenvector, we see that a_{11} and a_{33} have cosine values of approximately 0.4, showing that, in the model parameter space, the model parameters are not orthogonal to each other. As a result, error in estimating one parameter will leak into the estimation of another model parameter. The most challenging model parameter to recover is a_{33}. It is associated with the fifth eigenvector and eigenvalue, which is three orders of magnitude lower than the first eigenvalue.

Figure 4 shows eigenvectors and eigenvalues of the Hessian given that observed Rayleigh wave dispersion curve phase velocity includes the fundamental mode and the first higher mode. The eigenvector plot shows that a_{13} is better resolved relative to the case in which the Rayleigh wave dispersion curve included only fundamental mode phase velocities. Eigenvectors four and five show that including the first higher mode causes an increase in the interconnectivity between a_{11} and a_{33}. This implies that it will be harder to estimate a_{11} accurately relative to the case in which the Rayleigh wave dispersion mode includes only the fundamental mode. Errors in estimating a_{33}, which is associated with the lowest eigenvalue, will cause errors in a_{11} estimation. Figures 3 and 4 suggest that the general dispersion curve trend can be reproduced with a_{44} and n. Figure 4 suggests that when the observed Rayleigh wave dispersion curve includes the fundamental mode and the first higher mode, there is more interconnectivity between a_{11} and a_{33}.

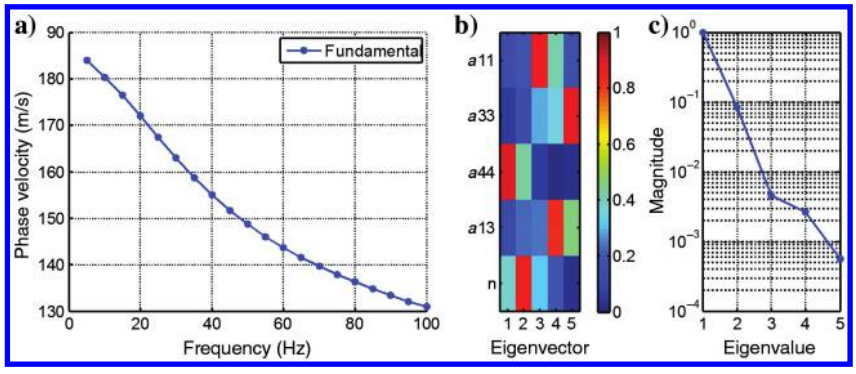

Figure 3. (a) Rayleigh wave dispersion curve made of the fundamental mode, (b) eigenvector matrix, and (c) logarithmic scaled plot of eigenvalues.

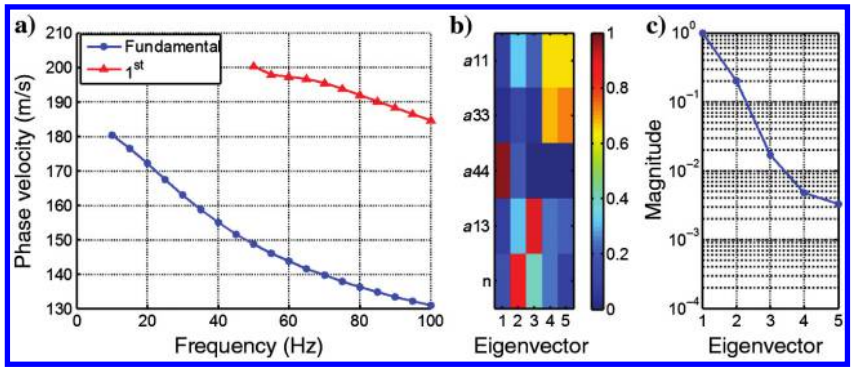

Figure 4. (a) Rayleigh wave dispersion curve made of the fundamental mode and first higher mode, (b) eigenvector matrix, and (c) logarithmic scaled plot of eigenvalues.

SURFACE-WAVE INVERSION METHOD

Inverting a Rayleigh wave dispersion curve is very challenging. The forward model operator is nonlinear, the model parameter sensitivity is complex, and the inversion solution is nonunique. As a result, gradient-based methods will converge to a local minima biased by the initial model (Luke et al., 2003; Dal Moro et al., 2007; Socco and Boiero, 2008). Therefore, prior to the inversion, we search for an initial model with a low data misfit to provide to the gradient-based solver.

We solve for the effective medium parameters in two steps. In step 1, we scan for the effective medium associated with the lowest data misfit between the modeled and the observed Rayleigh wave dispersion curves. This is done by initially calculating the depth-independent coefficients a_{11}, a_{33}, a_{44}, and a_{13} using Walton's (1987) equations. We calculate the coefficients for four different cases: a pack of infinitely rough spheres assuming a hydrostatic stress state, a pack of infinitely rough spheres assuming a uniaxial stress state, a pack of perfectly smooth spheres assuming a hydrostatic stress state, and a pack of perfectly smooth spheres assuming a uniaxial stress state. In each case, we scan for different values of porosity and coordination number, assuming we have prior information regarding the grains' elastic properties. We then calculate different Rayleigh wave dispersion curves for each set of a_{11}, a_{33}, a_{44}, and a_{13} given a different value of power-law depth dependency n. Zimmer et al. (2007) show that the power-law stress dependency of P- and S-wave velocity in dry sands can range from 1/3 to 1/6. This is equivalent to 1/1.5 to 1/3 power-law stress dependency of the effective elastic moduli. Therefore, we only model Rayleigh wave phase velocities for n ranging from 1.5 to 3. Finally, a misfit is calculated between the observed and the modeled dispersion curves.

In step 2, we use a quasi-Newton solver to minimize the objective function shown in equation C-1. The objective function is composed of two terms: The first term minimizes the fit to the observed data, and the second term penalizes deviation from the prior model. Note that the quasi-Newton method is dependent on an initial model and finds a local minimum. In this case, the initial model is the model with the lowest data misfit from step 1. This two-step approach does not require extensive scanning of the model parameter space and enables us to provide the Rayleigh wave inversion with a good starting model.

SYNTHETIC EXAMPLE

We test our surface-wave inversion by inverting an exact theoretical Rayleigh wave dispersion curve calculated for a sand model made of spherical quartz grains with the elastic parameters detailed in Table 1. First, we calculated the depth-independent coefficients for coordination numbers ranging from six to 10, with a sampling grid of 0.5, and then we modeled dispersion curves for each combination of the a_{ij} coefficients sets and n. In this example, we varied n values from two every 0.01 up to a maximum value of three. Figure 5 shows the fundamental mode of the true model (the black line with black circles) on top of the modeled curves color coded by their data misfit. In the figure, the modeled curve with the slowest phase velocities is associated with an a_{ij} set of effective medium with a coordination number of six and a uniaxial stress state. The modeled dispersion curve with the fastest phase velocities is related to an a_{ij} set of effective medium with a coordination number of 10 and a uniaxial stress state. The combination of calculated a_{ij} set, assuming porosity of 37%, a coordination number of nine and a power-law depth dependency of $n = 2.72$, generated the modeled curve with the lowest data misfit. Therefore, we chose this model to be the inversion's starting model. Its a_{ij} and the depth-power dependency values are detailed in Table 1. The effective medium values in Table 1 show that by scanning through different effective mediums, we were able to get an initial model that is very close to the true model.

Table 1. Rayleigh wave inversion results of synthetic example.

km^2/s^2	a_{11}	a_{33}	a_{44}	a_{13}	n
True model	0.79	2.03	0.24	0.52	2.80
Initial model	0.81	2.15	0.27	0.54	2.72
Inverted model	0.79	2.02	0.24	0.51	2.80

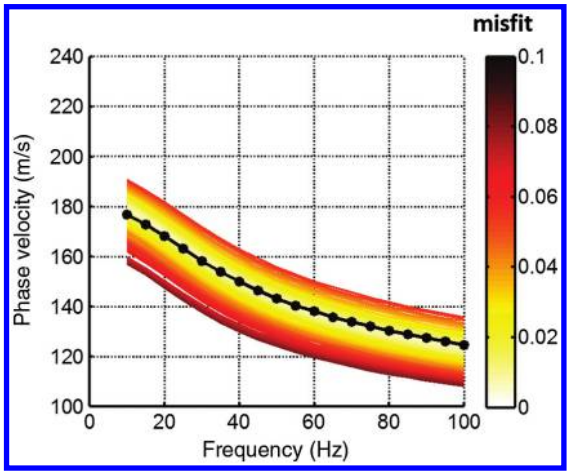

Figure 5. True model dispersion curve (black) and modeled dispersion curves of different effective granular mediums color coded by the data misfit.

Once we chose an initial model, we inverted the dispersion curve. In this synthetic example, we assumed no data uncertainty and that no prior information is available. The density is assumed to be constant and equal to the true model value. Figure 6 shows Rayleigh wave fundamental mode dispersion curves of the true model (blue line), the initial model (green line), and the inverted model (red line). Table 1 shows model parameters of the true model, the initial model, and the inverted model. Figure 6 shows the theoretical dispersion curve that was reproduced by inversion results, and Table 1 shows that all five model parameters were well-estimated. We see that the power-law depth dependency was accurately estimated. We also see in Table 1, that a_{33}, the hardest model parameter to recover, had only a 0.1 km/s^2 error. The synthetic example shows that we can solve for the effective medium of dry unconsolidated granular media using the proposed two-step approach.

REAL-DATA EXAMPLE

A multichannel analysis of surface wave (MASW) experiment was conducted on an Aeolian sand dune at Beit Yanai Beach, Israel. The sand comprises mainly of quartz grains with a mean diameter of 0.2 mm (Figure 8) and the in situ porosity was estimated to be 37%. A 2D seismic spread line with a 24 bit seismic acquisition system was placed 200 m from the water's edge on a dune. The line was composed of 96 27 Hz geophones with a group interval of 0.2 m. The seismic source was a 1.5 kg hammer hitting a flat aluminum plate. And the data were acquired by carrying out single-sensor recording. Figure 7a shows the seismic line placed on the sand and Figure 7b shows a microscopic image of a sand sample taken from the dune.

We created a shot supergather from all 25 shot locations along the seismic line by summing common-offset traces. The 1D assumption

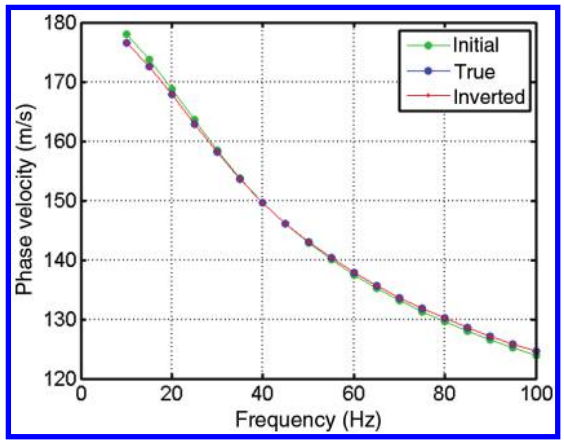

Figure 6. True model dispersion curve (blue line with circles), initial model dispersion curve (green line with circles), and inverted model dispersion curve (red line).

was validated by comparing picked dispersion curves from all different shots. Figure 8 shows a shot supergather and phase-velocity spectrum with the retrieved dispersion curve from a supergather. The fundamental mode can be picked from the velocity spectrum from 30 to 80 Hz, whereas higher modes are not visible within that range. Once we picked the dispersion curve, we compared it with dispersion curves modeled from the same granular media models used in the synthetic example. Figure 9 shows the picked phase velocities (black line with black circles) on top of the modeled curves color coded by their data misfit. The modeled curves are based on a_{ij} sets of the effective medium assuming a uniaxial stress state and perfectly smooth spheres. Following Gofer and Bachrach (2013), we chose a soft configuration with zero tangential stiffness. Note that because we had prior information on the in situ porosity, we limited our scanning to only the coordination number to calculate the depth-independent coefficients. The modeled fundamental mode curve with the smallest data misfit was calculated from an a_{ij} set, assuming a coordination number of 10. Murphy's (1982) coordination number for 37% porosity is about nine. The power-law depth dependency of the model is $n = 2.75$. This model was chosen as the inversion's starting model.

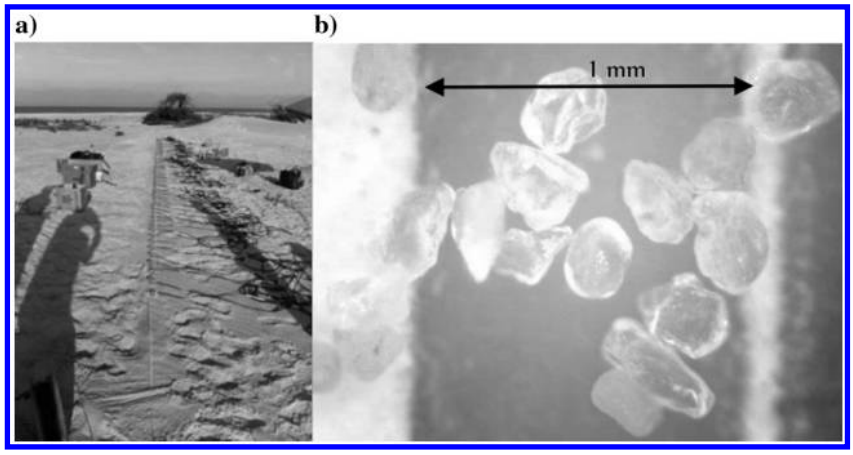

Figure 7. (a) The seismic line placed on the sand and (b) a microscopic image of a sample taken from the dune.

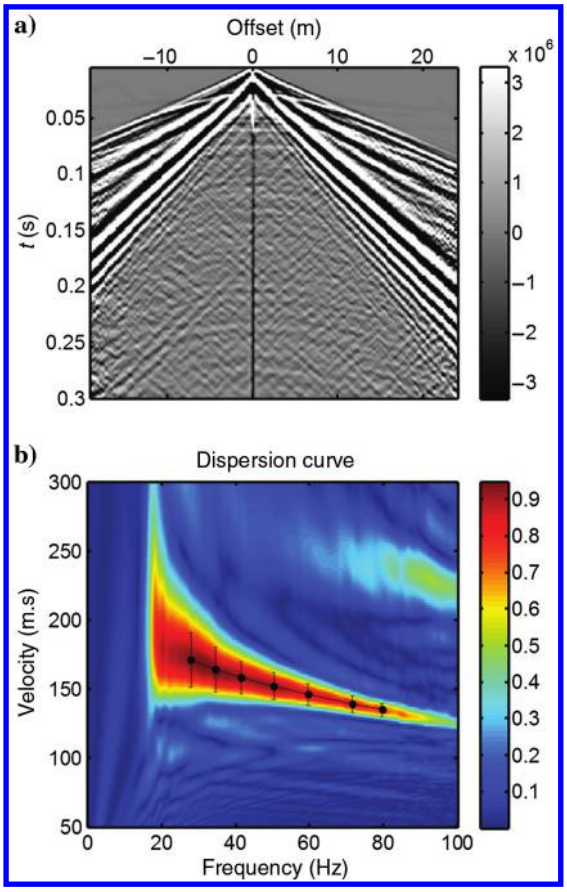

Figure 8. (a) Shot supergather and (b) observed phase-velocity spectrum and picked fundamental mode Rayleigh wave dispersion curve.

Table 2 shows inversion results of the five model parameters. Figure 10 shows the picked Rayleigh wave fundamental model (blue) and the modeled dispersion curve (red); the modeled effective elastic medium based on inversion results is plotted in Figure 11. Figure 10 shows that the observed dispersion curve is well-fitted by the inverted dispersion curve. The inversion results shown in Table 2 show a sand model of $a_{11} = 1.17$ (km/s)^2, $a_{33} = 2.6$ (km/s)^2, $a_{44} = 0.39$ (km/s)^2, and $a_{13} = 0.14$ (km/s)^2 with a power dependence in depth of 1/2.43.

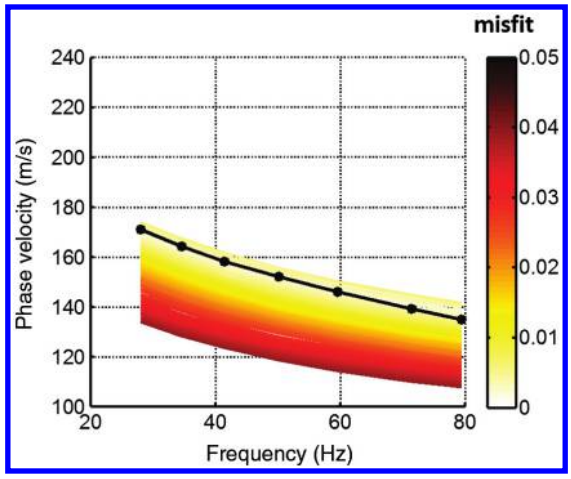

Figure 9. Picked Rayleigh wave dispersion curve (black) and modeled dispersion curves of different effective granular mediums color coded by data misfit.

Table 2. Rayleigh wave inversion results of real-data example.

km^2/s^2	a_{11}	a_{33}	a_{44}	a_{13}	n
Initial model	0.86	2.30	0.29	0.57	2.75
Inverted model	1.17	2.60	0.39	0.14	2.43

COMPARISON WITH PREVIOUS RESULTS FOR GRANULAR MEDIA

The inverted results are in agreement with Zimmer et al. (2007), who showed that, at low effective stress, the P- and S-wave velocities stress dependency varies from 1/4 to 1/6. This is equivalent to 1/2 to 1/3 power-law dependency of the effective elastic parameters. Walton (1987) predicts a 1/3 power-law dependence assuming that all spheres are identical, have constant porosity, and a constant coordination number. This discrepancy was attributed in the past to an increase in coordination number with an increase in effective stress and buckling of particle chains (Goddard, 1990; Cascante and Santamarina, 1996).

Based on inverted a_{33} and a_{44}, we calculated a 2.58 V_P/V_S ratio. The calculated ratio is high when compared with values observed by previous publications using isotropic assumptions. In works by Bachrach et al. (2000), Jacob et al. (2008), and Bodet et al. (2010), all V_P/V_S ratios range from 1.5 to 2. This result is more comparable with ratios calculated by Zimmer (2003). At low effective stress, Zimmer (2003) calculates a V_P/V_S ratio ranging up to 2.6. Note that Bachrach et al. (2000) estimate Poisson's ratio based on the best-fitted Hertz-Mindlin model by taking into account grain angularity and assuming that the media consists of slipping and nonslipping grain contacts. Zimmer (2003), Jacob et al. (2008), and Bodet et al. (2010) estimate the stress-independent coefficient and power-law stress dependency for P- and S-velocity individually. The results shown here estimated four of the five VTI elastic constants given a single power-law dependence.

Thomsen's (1986) ε and δ from the surface-wave inversion results were calculated to be $\varepsilon = -0.28$ and $\delta = -0.39$. A value of $\varepsilon = -0.3$ was obtained from velocity measurements from uniaxial compression testing on dry Santa Crus sand by Ruiz (2003). The sand sample had high porosity of 0.45, mean grain size of 0.25 mm, and grain density of 2.606. These values are similar to the Aeolian sand on which the seismic experiment was carried out. The VTI model inverted from Rayleigh wave dispersion indicates that the medium is stiffer along the vertical axis than the horizontal axis.

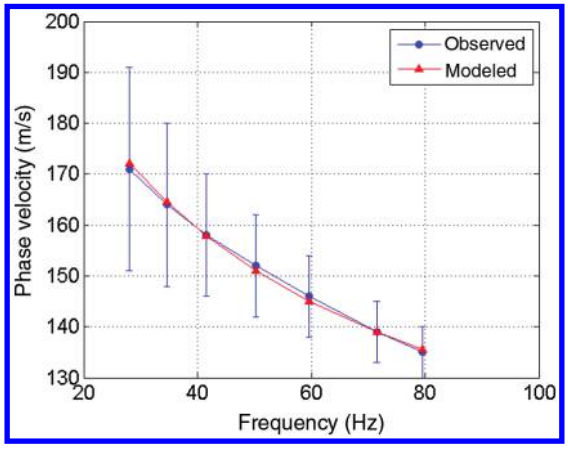

Figure 10. Picked Rayleigh wave dispersion curve (blue) and modeled Rayleigh wave dispersion curve (red). Modeled dispersion curve is based on inversion results.

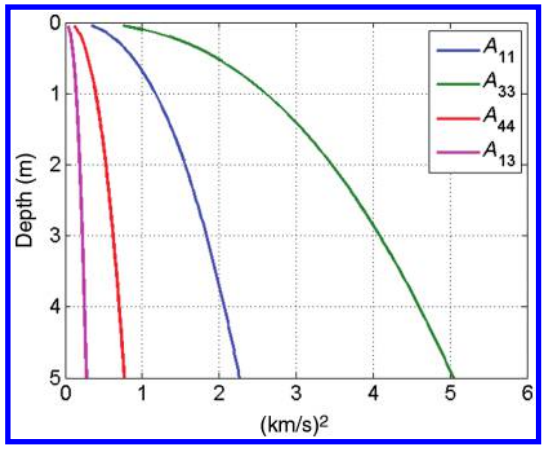

Figure 11. Effective density normalized elastic stiffnesses as a function of depth based on surface-wave inversion results.

CONCLUSION

We introduced an anisotropic Rayleigh wave inversion that solves for an in situ effective elastic medium in unconsolidated dry sands. The inversion solves for depth-independent coefficients of density-normalized elastic parameters A_{11}, A_{33}, A_{44}, and A_{13} and for their power dependency in depth. We demonstrated on a synthetic example that we are able to solve for all five parameters by inverting fundamental mode and incorporating rock-physics modeling to obtain a good initial model. We also showed surface-wave inversion results from a MASW experiment on an Aeolian sand dune. We were able to estimate the in situ 1D profile of the effective elastic medium. The estimated power dependency in depth 1/2.43 is in agreement with published observations. Inversion results also show that the in situ V_P/V_S ratio is high, 2.58, and that Thomsen's ε and δ have values of approximately -0.3. Results indicate that the sand is elastically anisotropic and that it is stiffer along the vertical axis than the horizontal axis.

Anisotropic Rayleigh wave inversion can provide a better insight of in situ elastic properties in unconsolidated granular media than isotropic Rayleigh wave inversion. Solving for four independent elastic parameters A_{11}, A_{33}, A_{44}, and A_{13} and their power dependence in depth makes Rayleigh wave inversion a more robust tool to characterize in situ granular media. We acknowledge that, to carry out better characterization of granular media, we must further expand the methodology presented here. Our initial model search is constrained by the limitation of the Walton model. We can only calculate effective elastic moduli for either a hydrostatic stress state or a uniaxial stress state, and we are limited to have prior information on the grain composition of the unconsolidated rock. We must also further develop our method performing joint anisotropic Rayleigh wave and Love wave inversion as well as joint anisotropic surface wave and guided wave inversion. Love waves are a function of A_{44} and A_{66}. A joint inversion will enable us to estimate A_{44} more accurately. Moreover, we will be able solve for all five independent VTI elastic parameters. Joint anisotropic surface wave and guided wave inversion might help to improve the accuracy of the estimated A_{11} and A_{33}.

ACKNOWLEDGMENTS

The authors would like to thank J. Shragge, A. Baumstein, V. Socco, and two anonymous reviewers for their constructive comments that helped to improve this paper.

APPENDIX A

ANISOTROPIC THOMSON-HASKELL MATRIX

Here, we present the explicit analytical expression of matrix **A**'s eigenvalues, eigenvectors (matrix **F**), and matrix **G**. To do so, we begin by defining several terms:

$$\chi = A_{11}A_{33} - A_{13}^2, \tag{A-1}$$

$$\alpha = k^4\chi(2 * A_{44} + A_{13}), \tag{A-2}$$

$$\beta = -(k^2\omega^2)(2A_{33}A_{44} + A_{13}A_{33} + 3A_{13}A_{44} + 2A_{13}^2 - \chi), \tag{A-3}$$

$$\gamma = \omega^4(A_{33} - A_{44}), \tag{A-4}$$

$$\begin{aligned}\zeta_1 &= 2k^4\chi(A_{44} + A_{13}) - k^2\omega^2(2A_{33}A_{44} + A_{13}A_{33} + 3A_{13}A_{44} \\ &\quad + 2A_{13}^2 + \chi) + \omega^4(A_{33} - A_{44}) + \sqrt{\alpha + \beta + \gamma}, \\ \zeta_2 &= 2k^4\chi(A_{44} + A_{13}) - k^2\omega^2(2A_{33}A_{44} + A_{13}A_{33} + 3A_{13}A_{44} \\ &\quad + 2A_{13}^2 + \chi) + \omega^4(A_{33} - A_{44}) - \sqrt{\alpha + \beta + \gamma},\end{aligned} \tag{A-5}$$

where A_{ij} are the density normalized elastic stiffnesses, k is the wavenumber, and ω is the angular frequency.

The square of the eigenvalues of matrix **A** are defined as

$$\begin{aligned}\lambda_1^2 &= \frac{\left[-k^2A_{13}A_{44} + \frac{1}{2}(k^2\chi - \omega^2(A_{33} + A_{44}) + \sqrt{\alpha + \beta + \gamma})\right]}{A_{33}A_{44}}; \\ \lambda_2^2 &= \frac{\left[-k^2A_{13}A_{44} + \frac{1}{2}(k^2\chi - \omega^2(A_{33} + A_{44}) - \sqrt{\alpha + \beta + \gamma})\right]}{A_{33}A_{44}}.\end{aligned} \tag{A-6}$$

Matrix **A**'s eigenvector are

$$\begin{aligned}F_{11} &= \left[A_{44}^2\zeta_1 + \left(k^2\chi(2A_{33} + A_{13}) - \omega^2\left(2A_{33}A_{44} + A_{13}(A_{33} + A_{44})\right.\right.\right. \\ &\quad \left.\left.\left. + A_{13}\sqrt{\alpha + \beta + \gamma}\right)\right)\right]\left[k^2A_{13}A_{44} - 0.5\left(k^2\chi - \omega^2(A_{33} + A_{44})\right.\right. \\ &\quad \left.\left. + \sqrt{\alpha + \beta + \gamma}\right)\right] \\ &\quad \times\left[\left(k^2\chi - \omega^2(A_{33} + A_{44}) + \sqrt{\alpha + \beta + \gamma}\right)\right]^{-1}\zeta_1^{-1}, \\ F_{21} &= -\lambda_1A_{44}k^{-1}\left[k^2A_{13}\zeta_1^{-1}\left(A_{44}^2\zeta_1 + \left(k^2\chi(2A_{33} + A_{13}) - \omega^2\right.\right.\right. \\ &\quad \left.\left.\left. \times\left(2A_{33}A_{44} + A_{13}(A_{33} + A_{44}) + A_{13}\sqrt{\alpha + \beta + \gamma}\right)\right)\right) + A_{44}\right] \\ &\quad \times\left[(k^2\chi - \omega^2(A_{33} + A_{44}) + \sqrt{\alpha + \beta + \gamma})\right]^{-1}, \\ F_{31} &= 0.5\lambda_1A_{44}\rho\zeta_1^{-1}\left[k^2\chi(2A_{44} + A_{13}) - \omega^2\right. \\ &\quad \left.\times\left(2A_{33}A_{44} + A_{13}(A_{33} + A_{44}) + A_{13}\sqrt{\alpha + \beta + \gamma}\right)\right], \\ F_{41} &= 0.5A_{44}\rho k^{-1}, \\ F_{12} &= \left[A_{44}^2\zeta_2 + \left(k^2\chi(2A_{33} + A_{13}) - \omega^2\left(2A_{33}A_{44} + A_{13}(A_{33} + A_{44})\right.\right.\right. \\ &\quad \left.\left.\left. + A_{13}\sqrt{\alpha + \beta + \gamma}\right)\right)\right]\left[k^2A_{13}A_{44} - 0.5\right. \\ &\quad \left.\times\left(k^2\chi - \omega^2(A_{33} + A_{44}) + \sqrt{\alpha + \beta + \gamma}\right)\right] \\ &\quad \times\left[\left(k^2\chi - \omega^2(A_{33} + A_{44}) + \sqrt{\alpha + \beta + \gamma}\right)\right]^{-1}\zeta_2^{-1}, \\ F_{22} &= -\lambda_2A_{44}k^{-1}\left[k^2A_{13}\zeta_2^{-1}\left(A_{44}^2\zeta_2 + \left(k^2\chi(2A_{33} + A_{13}) - \omega^2\right.\right.\right. \\ &\quad \left.\left.\left. \times\left(2A_{33}A_{44} + A_{13}(A_{33} + A_{44}) + A_{13}\sqrt{\alpha + \beta + \gamma}\right)\right)\right) + A_{44}\right] \\ &\quad \times\left[\left(k^2\chi - \omega^2(A_{33} + A_{44}) + \sqrt{\alpha + \beta + \gamma}\right)\right]^{-1}, \\ F_{32} &= 0.5\lambda_1A_{44}\rho\zeta_2^{-1}\left[k^2\chi(2A_{44} + A_{13}) - \omega^2\right. \\ &\quad \left.\times\left(2A_{33}A_{44} + A_{13}(A_{33} + A_{44}) + A_{13}\sqrt{\alpha + \beta + \gamma}\right)\right] \\ F_{42} &= 0.5A_{44}\rho k^{-1},\end{aligned} \tag{A-7}$$

where matrix **F** is

$$\mathbf{F} = \begin{bmatrix} F_{11} & F_{12} & F_{11} & F_{12} \\ F_{21} & F_{22} & -F_{21} & -F_{22} \\ F_{31} & F_{32} & -F_{31} & -F_{32} \\ F_{41} & F_{42} & F_{41} & F_{42} \end{bmatrix}. \tag{A-8}$$

At this point, we define another quantity that is a function of the eigenvalues and will be used when we define matrix **G**:

$$\kappa = (\lambda_1 - \lambda_2)(\lambda_1 + \lambda_2). \tag{A-9}$$

The components of matrix $\mathbf{G}$ for each layer are

$$\mathbf{G}_{11}=\mathbf{G}_{33}=(k^2[\chi(A_{33}A_{44})^{-1}-A_{13}A_{33}^{-1}-\omega^2A_{44}^{-1}][\cosh(\lambda_1 h)-\cosh(\lambda_2 h)]+\lambda_1^2\cosh(\lambda_2 h)-\lambda_2^2\cosh(\lambda_1 h))\kappa^{-1},$$

$$\mathbf{G}_{12}=-\mathbf{G}_{43}=\begin{pmatrix}[k^3(\chi(A_{33}A_{44})-A_{13}A_{33}-k^{-2}\omega^2A_{44}-k^{-2}\lambda_2^2)-k\omega^2A_{33}^{-1}(1+A_{13}A_{44})]\lambda_1\sinh(\lambda_1 h)-\\ [k^3(\chi(A_{33}A_{44})-A_{13}A_{33}-k^{-2}\omega^2A_{44}-k^{-2}\lambda_1^2)-k\omega^2A_{33}^{-1}(1+A_{13}A_{44})]\lambda_2\sinh(\lambda_2 h)\end{pmatrix}\kappa^{-1},$$

$$\mathbf{G}_{13}=\begin{pmatrix}[-k^2A_{33}^{-1}(\rho^{-1}+A_{13}(A_{44}\rho)^{-1})+(k^2[\chi(A_{33}A_{44})^{-1}-A_{13}A_{33}^{-1}]-\omega^2A_{44}^{-1}-\lambda_2^2)]\lambda_1\sinh(\lambda_1 h)-\\ [-k^2A_{33}^{-1}(\rho^{-1}+A_{13}(A_{44}\rho)^{-1})+(k^2[\chi(A_{33}A_{44})^{-1}-A_{13}A_{33}^{-1}]-\omega^2A_{44}^{-1}-\lambda_1^2)]\lambda_2\sinh(\lambda_2 h)\end{pmatrix}\kappa^{-1},$$

$$\mathbf{G}_{14}=-\mathbf{G}_{23}=[kA_{33}^{-1}(1+A_{13}A_{44}^{-1})(\cosh(\lambda_1 h)-\cosh(\lambda_2 h))](\kappa\rho)^{-1},$$

$$\mathbf{G}_{21}=\mathbf{G}_{34}=\begin{bmatrix}(kA_{13}A_{33}(k^2A_{13}A_{33}^{-1}+\omega^2A_{33}^{-1}+\lambda_2^2)-kA_{33}^{-1}(k^2\chi A_{33}^{-1}-\omega^2)(1+A_{13}A_{44}^{-1}))\lambda_1^{-1}\sinh(\lambda_1 h)-\\ (kA_{13}A_{33}(k^2A_{13}A_{33}^{-1}+\omega^2A_{33}^{-1}+\lambda_1^2)-kA_{33}^{-1}(k^2\chi A_{33}^{-1}-\omega^2)(1+A_{13}A_{44}^{-1}))\lambda_2^{-1}\sinh(\lambda_2 h)\end{bmatrix}(\kappa\rho)^{-1},$$

$$\mathbf{G}_{22}=\mathbf{G}_{44}=[(k^2A_{13}A_{33}^{-1}-\omega^2A_{33}+\lambda_1^2)\cosh(\lambda_2 h)-(k^2A_{13}A_{33}^{-1}-\omega^2A_{33}+\lambda_2^2)\cosh(\lambda_1 h)]\kappa^{-1},$$

$$\mathbf{G}_{24}=\begin{bmatrix}(-k^2A_{13}A_{33}^{-2}\rho^{-1}(1+A_{13}A_{44}^{-1})-A_{33}^{-1}\rho^{-1}(k^2A_{13}A_{33}^{-1}-\omega^2A_{33}^{-1}-\lambda_2^2))\lambda_1^{-1}\sinh(\lambda_1 h)-\\ (-k^2A_{13}A_{33}^{-2}\rho^{-1}(1+A_{13}A_{44}^{-1})-A_{33}^{-1}\rho^{-1}(k^2A_{13}A_{33}^{-1}-\omega^2A_{33}^{-1}-\lambda_1^2))\lambda_2^{-1}\sinh(\lambda_2 h)\end{bmatrix}\kappa^{-1},$$

$$\mathbf{G}_{31}=\begin{bmatrix}(-(k^2A_{13}\rho A_{33}^{-1})(k^2\chi A_{33}-\omega^2-\omega^2A_{13}A_{33}^{-1})+(k^2\chi\rho A_{33}-\omega^2\rho)(-k^2A_{13}A_{33}^{-1}+k^2\chi A_{33}^{-1}A_{44}^{-1})-\omega^2A_{44}^{-1}-\lambda_2^2)\lambda_1\sinh(\lambda_1 h)-\\ (-(k^2A_{13}\rho A_{33}^{-1})(k^2\chi A_{33}-\omega^2-\omega^2A_{13}A_{33}^{-1})+(k^2\chi\rho A_{33}-\omega^2\rho)(-k^2A_{13}A_{33}^{-1}+k^2\chi A_{33}^{-1}A_{44}^{-1})-\omega^2A_{44}^{-1}-\lambda_1^2)\lambda_2\sinh(\lambda_2 h)\end{bmatrix}\kappa^{-1},$$

$$\mathbf{G}_{32}=-\mathbf{G}_{41}=[k\rho(k^2\chi A_{33}^{-1}-\omega^2-\omega^2A_{13}A_{33}^{-1})(\cosh(\lambda_1 h)-\cosh(\lambda_2 h))]\kappa^{-1},$$

$$\mathbf{G}_{42}=\begin{bmatrix}(-k^4\chi A_{33}^{-1}+k^2\omega^2(1+2A_{33}^{-1})+\omega^4A_{33}^{-1}+\omega^2\lambda_2^2)\lambda_1^{-1}\sinh(\lambda_1 h)-\\ (-k^4\chi A_{33}^{-1}+k^2\omega^2(1+2A_{33}^{-1})+\omega^4A_{33}^{-1}+\omega^2\lambda_1^2)\lambda_2^{-1}\sinh(\lambda_2 h)\end{bmatrix}\kappa^{-1}\rho. \tag{A-10}$$

APPENDIX B

REVIEW OF GRANULAR MEDIA EFFECTIVE MEDIUM APPROXIMATION

Walton (1987) explicitly expresses effective elastic moduli for a random packing of identical spheres corresponding to the hydrostatic stress state and the uniaxial stress state, where the spheres are assumed to be either infinitely rough or perfectly smooth. For the hydrostatic stress case, unconsolidated media can be assumed to be statistically isotropic. Therefore, its effective stiffness tensor can be represented using two effective elastic moduli, bulk and shear modulus. For a pack of perfectly smooth spheres, the bulk and the shear modulus are defined as

$$G_{\text{eff}}=\frac{1}{10}\left(\frac{3(1-\varphi)^2c^2\langle P\rangle}{\pi^4B^2}\right)^{1/3};\quad K_{\text{eff}}=\frac{5}{3}G_{\text{eff}}, \tag{B-1}$$

where φ, c, and $\langle P\rangle$ are the porosity, coordination number, and the effective hydrostatic stress, respectively; B is derived directly from the grains' Lamé moduli, λ and n

$$B=\frac{1}{4\pi}\left(\frac{1}{\mu}+\frac{1}{\lambda+\mu}\right), \tag{B-2}$$

where the grains are assumed to be made of isotropic mineral.

When the same granular pack is subjected to uniaxial stress along the vertical direction, the vertical strain is then defined by

$$-e_3=-\left(\frac{\langle\sigma_3\rangle 6\pi^2B}{(1-\varphi)n}\right)^{2/3}. \tag{B-3}$$

Under uniaxial compression, the medium is statistically transversely isotropic, which can be described by five independent elastic constants C_{11}, C_{33}, C_{44}, C_{66}, and C_{13}. For a pack of perfectly smooth spheres, the effective moduli are given by

$$C_{11}=3\alpha; C_{33}=8\alpha; C_{44}=\alpha; C_{66}=\alpha; C_{13}=2\alpha, \tag{B-4}$$

where α is

$$\alpha=\frac{(1-\varphi)c(-e_3)^{1/2}}{32\pi^2B}. \tag{B-5}$$

Equation B-4 shows that, for granular packs under uniaxial loading, $C_{33}>C_{11}$.

We assume that the vertical effective stress in unconsolidated dry sands is the overburden stress

$$\sigma_{OB}=\int_0^z\rho(z)g dz, \tag{B-6}$$

where $\rho(z)$ is the density at depth z and g is the acceleration due to gravity. Using equations B-1 through B-5, we can calculate the effective elastic moduli at each depth point using uniaxial and/or hydrostatic loading conditions.

APPENDIX C

REVIEW OF BAYESIAN INVERSION UNCERTAINTY ANALYSIS

Formulating an inverse problem as a Bayesian inverse problem, in which the posterior PDF is defined as $p(\mathbf{m}/\mathbf{d})\propto p(\mathbf{d}|\mathbf{m})p(\mathbf{m})$, the objective function, assuming normal distribution, is then given by (Duijndam, 1988):

$$J(\mathbf{m})=\frac{1}{2}(\mathbf{d}-\mathbf{G}(\mathbf{m}))C_d^{-1}(\mathbf{d}-\mathbf{G}(\mathbf{m}))+\frac{1}{2}(\mathbf{m}_0-\mathbf{m})C_m^{-1}(\mathbf{m}_0-\mathbf{m}), \tag{C-1}$$

where $\mathbf{d}$ is the picked Rayleigh wave dispersion curve, $\mathbf{m}_0$ is the prior model, and C_m and C_d are the data and prior model covariance matrices, respectively. In the region where $J(\mathbf{m})$ is close to its minimum, $J(\hat{\mathbf{m}})$, $J(\mathbf{m})$ can be expended in a Taylor series (Brad, 1974)

$$J(\mathbf{m})=J(\hat{\mathbf{m}})+\frac{\partial J}{\partial m_i}\Delta\mathbf{m}+\frac{1}{2}\Delta\mathbf{m}^T\frac{\partial^2J}{\partial m_i\partial m_j}\Delta\mathbf{m}, \tag{C-2}$$

where $\Delta\mathbf{m}=\mathbf{m}-\hat{\mathbf{m}}$. At the minimum, the gradient, $\partial J/\partial m_i$, vanishes and the region around the minimum is then expressed by the Hessian as

$$2[J(\mathbf{m})-J(\hat{\mathbf{m}})]=\Delta\mathbf{m}^T\frac{\partial^2J}{\partial m_i\partial m_j}\Delta\mathbf{m}. \tag{C-3}$$

The shape of equation C-3 is an N-dimensional ellipsoid. We can approximate the shape of the ellipsoid without the requirement to map the a posteriori PDF with eigenvalue decomposition of the Hessian:

$$\frac{\partial^2J}{\partial m_i\partial m_j}=\mathbf{V}\mathbf{\Lambda}^2\mathbf{V}^T, \tag{C-4}$$

where $\mathbf{V}$ is the normalized eigenvector matrix and $\mathbf{\Lambda}$ is a vector of the eigenvalues. The principle axes of the ellipsoid correspond to the coordinate axes of the eigenvectors of the Hessian, and the length in which the ellipsoid stretches along these axes is inversely proportional to the square roots of the eigenvalues. This means that

the ellipsoid stretches further in the directions associated with low eigenvalues where the model parameters are poorly resolved (Duijndam, 1988).

REFERENCES

Aki, K., and P. G. Richards, 1980, Quantitative seismology: H. W. Freeman and Co.

Anderson, D. L., 1961, Elastic wave propagation in layered anisotropic media: Journal of Geophysical Research, **66**, 2953–2963, doi: 10.1029/JZ066i009p02953.

Bachrach, R., J. Dvorkin, and A. M. Nur, 1998, High-resolution shallow-seismic experiments in sand. Part II: Velocities in shallow unconsolidated sand: Geophysics, **63**, 1234–1240, doi: 10.1190/1.1444424.

Bachrach, R., J. Dvorkin, and A. M. Nur, 2000, Seismic velocities and Poisson's ratio of shallow unconsolidated sands: Geophysics, **65**, 559–564, doi: 10.1190/1.1444751.

Bergamo, P., and L. V. Socco, 2016, P- and S-wave velocity models of shallow dry sand formations from surface wave multimode inversion: Geophysics, **81**, no. 4, R197–R209, doi: 10.1190/geo2015-0542.1.

Bodet, L., X. Jacob, and V. Tournat, 2010, Elasticity profile of an unconsolidated granular medium inferred from guided waves: Toward acoustic monitoring of analogue models: Tectonophysics, **496**, 99–104, doi: 10.1016/j.tecto.2010.10.004.

Brad, Y., 1974, Nonlinear parameter estimation: Academic Press.

Cascante, G., and J. C. Santamarina, 1996, Interparticle contact behavior and wave propagation: Journal of Geotechnical Engineering, **122**, 831–839, doi: 10.1061/(ASCE)0733-9410(1996)122:10(831).

Dal Moro, G., M. Pipan, and P. Gabrielli, 2007, Rayleigh wave dispersion curve inversion via genetic algorithms and marginal posterior probability density estimation: Journal of Applied Geophysics, **61**, 39–55, doi: 10.1016/j.jappgeo.2006.04.002.

Digby, P. J., 1981, The effective elastic moduli of porous granular rocks: Journal of Applied Mechanics, **48**, 803–808, doi: 10.1115/1.3157738.

Duijndam, A., 1988, Bayesian estimation in seismic inversion. Part II: Uncertainity analysis: Geophysical Prospecting, **36**, 899–918, doi: 10.1111/j.1365-2478.1988.tb02199.x.

Duijndam, A. J. W., 1988, Bayesian estimation in seismic inversion. Part I: Principles: Geophysical Prospecting, **36**, 878–898, doi: 10.1111/j.1365-2478.1988.tb02198.x.

Geng, J., D. Howell, E. Longhi, R. P. Behringer, G. Reydellet, L. Vanel, E. Clement, and S. Luding, 2001, Footprints in sand: The response of a granular material to local perturbations: Physical Review Letters, **87**, 355061–355064, doi: 10.1103/PhysRevLett.87.035506.

Gilbert, F., and G. Backus, 1966, Propagator matrices in elastic wave and vibration problems: Geophysics, **31**, 326–332, doi: 10.1190/1.1439771.

Goddard, J. D., 1990, Nonlinear elasticity and pressure-dependent wave speeds in granular media: Proceedings of the Royal Society A: Mathematical, Physical and Engineering Sciences, **430**, 105–131, doi: 10.1098/rspa.1990.0083.

Gofer, E., and R. Bachrach, 2012, In situ shear modulus in granular media: A surface wave inversion approach: 74th Annual International Conference and Exhibition, EAGE, Extended Abstracts, 121–124.

Gofer, E., and R. Bachrach, 2013, Surface wave anisotropy in granular media: Comparison between numerical tests and field data: 83rd Annual International Meeting, SEG, Expanded Abstracts, 1771–1775.

Haskel, N. A., 1953, The dispersion of surface wave on multilayered media: Bulletin of the Seismological Society of America, **43**, 17–34.

Jacob, X., V. A. Tournat, P. Leclaire, W. Lauriks, and V. E. Gusev, 2008, Acoustic probing of the jamming transition in an unconsolidated granular medium: Physical Review Letters, **100**, 158003, doi: 10.1103/PhysRevLett.100.158003.

Ke, G., H. Dong, A. Kristensen, and M. Thmopson, 2011, Modified Thomson-Haskell matrix methods for surface-wave dispersion-curve calculation and their accelerated root-searching schemes: Bulletin of the Seismological Society of America, **101**, 1692–1703, doi: 10.1785/0120100187.

Luke, B., C. Calderón, R. C. Stone, and M. Huynh, 2003, Non-uniqueness in inversion of seismic surface-wave data: Proceedings of Symposium on the Application of Geophysics to Engineering and Environmental Problems (SAGEEP), Environmental and Engineering Geophysical Society, 1342–1347.

Murphy, W. F., 1982, Effect of microstructure and pore fluids on the acoustic properties of granular sedimentary materials: Ph.D. dissertation, Stanford University.

Nur, A. M., and G. Simmones, 1969, Stress-induced velocity anisotropy in rock: An experimental study: Journal of Geophysical Research, **74**, 6667–6674, doi: 10.1029/JB074i027p06667.

Ruiz, D. S. V., 2003, Intrinsic and stress-induced velocity anisotropy in unconsolidated sands: Ph.D. dissertation, Stanford University.

Sayers, C., 2002, Stress-dependent elastic anisotropy of sandstones: Geophysical Prospecting, **50**, 85–95, doi: 10.1046/j.1365-2478.2002.00289.x.

Socco, L. V., and D. Boiero, 2008, Improved Monte Carlo inversion of surface wave data: Geophysical Prospecting, **56**, 357–371, doi: 10.1111/j.1365-2478.2007.00678.x.

Thomsen, L., 1986, Weak elastic anisotropy: Geophysics, **51**, 1954–1966, doi: 10.1190/1.1442051.

Thomson, W. T., 1950, Transmission of elastic waves through a stratified solid medium: Journal of Applied Physics, **21**, 89–93, doi: 10.1063/1.1699629.

Walton, K., 1987, The effective elastic moduli of a random packing of spheres: Journal of the Mechanics and Phyiscs of Solids, **35**, 213–226, doi: 10.1016/0022-5096(87)90036-6.

Zimmer, M. A., 2003, Seismic velocities in unconsolidated sands: Measurements of pressure, sorting, and compaction effects: Ph.D. dissertation, Stanford University.

Zimmer, M. A., M. Prasad, and G. Mavko, 2002, Empirical velocity-pressure and porosity-pressure trends in unconsolidated sands: 72nd Annual International Meeting, SEG, Expanded Abstracts, 1866–1869.

Zimmer, M. A., M. Prasad, and G. Mavko, 2007, Seismic velocities of unconsolidated sands. Part 1: Pressure trends from 0.1 to 20 MPa: Geophysics, **72**, no. 1, E1–E13, doi: 10.1190/1.2399459.